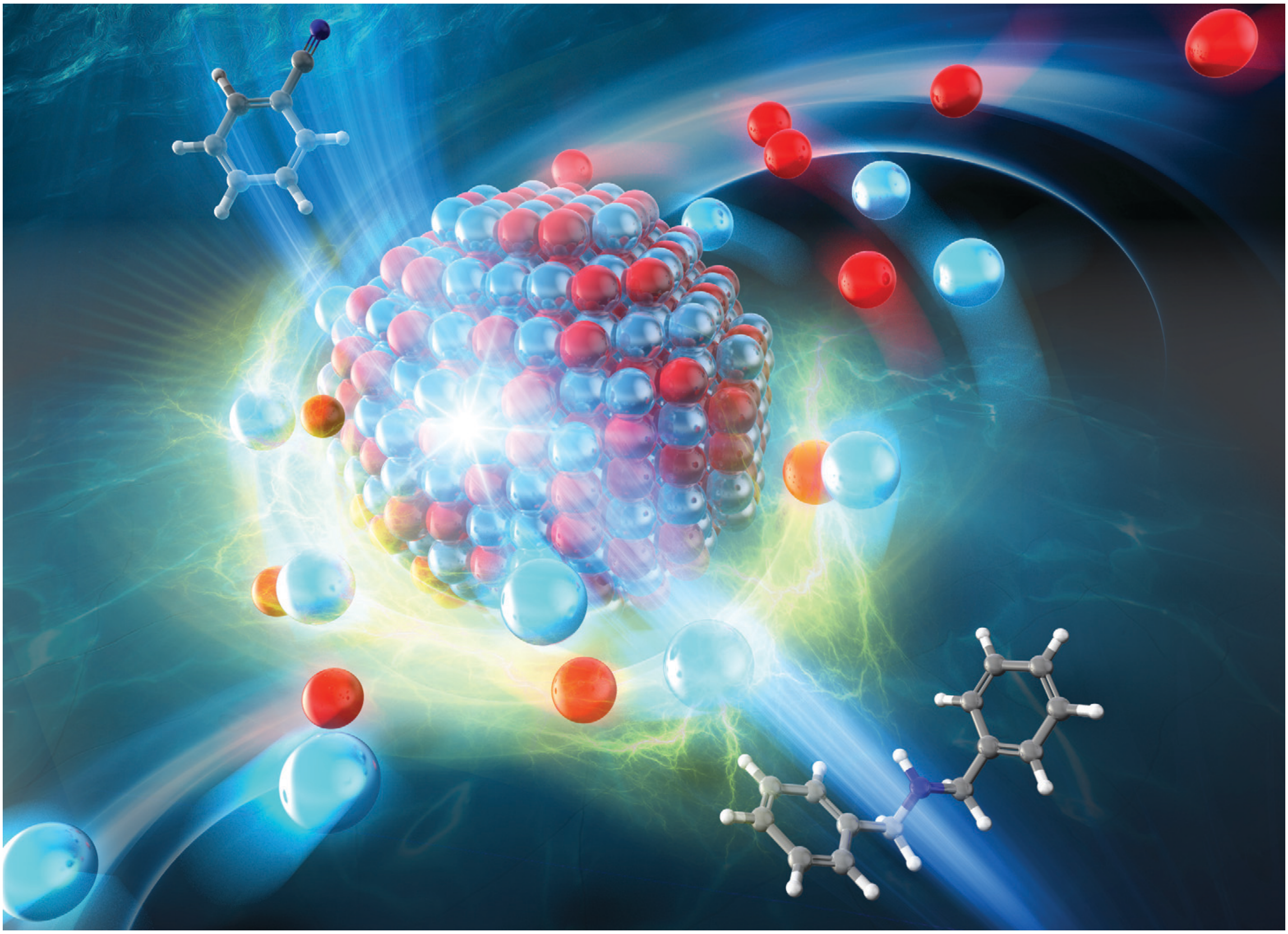

Showcasing research from Professor Katsutoshi Nagaoka's laboratory, Department of Chemical Systems Engineering, Graduate School of Engineering, Nagoya University, Nagoya, Japan.

Nitrile hydrogenation to secondary amines under ambient conditions over palladium–platinum random alloy nanoparticles

Palladium-platinum random alloy nanoparticles enable hydrogenation of nitriles to secondary amines without the need for heat, pressurization, or long reaction times. Although palladium and platinum are classically immiscible, they were successfully alloyed through rapid chemical reduction assisted by microwave heating. The palladium-platinum random alloy nanoparticles exhibited 10-fold higher turnover frequency than the monometallic palladium and platinum nanoparticles, and were able to facilitate the conversion of various nitriles to the corresponding secondary amines.

As featured in:

Catalysis Science & Technology

See Yoshihide Nishida, Katsutoshi Sato, Katsutoshi Nagaoka *et al.*, *Catal. Sci. Technol.*, 2022, **12**, 4128.

ROYAL SOCIETY OF **CHEMISTRY**

rsc.li/catalysis

Catalysis Science & Technology

ROYAL SOCIETY OF CHEMISTRY

PAPER

View Article Online
View Journal | View Issue

Check for updates

Cite this: *Catal. Sci. Technol.*, 2022, **12**, 4128

Nitrile hydrogenation to secondary amines under ambient conditions over palladium–platinum random alloy nanoparticles†

Yoshihide Nishida, ‡*[a] Katsutoshi Sato, *[ab] Chandan Chaudhari,§[a]
Hiroshi Yamada,[a] Takaaki Toriyama,[c] Tomokazu Yamamoto,[d] Syo Matsumura,[cd]
Susan Meñez Aspera, [e] Hiroshi Nakanishi, [e]
Masaaki Haneda [fg] and Katsutoshi Nagaoka *[a]

Catalytic hydrogenation of nitriles is a cost-effective and green method for synthesizing amines and imines, which have many industrial applications. However, this reaction generally requires harsh reaction conditions and produces a mixture of amine and imine products due to its chemodiversity. Therefore, it is a challenge to selectively hydrogenate nitriles to a single product under ambient conditions (1 bar of H_2 at 25 °C). Here, we report an effective method for selective hydrogenation of nitriles that does not require heat, pressurization, or long reaction times. We achieved this by means of bimetalization between palladium (Pd) and platinum (Pt) nanoparticles, which resulted in a catalyst that showed high yield of secondary amines. Although Pd and Pt are thermodynamically immiscible, we have successfully alloyed the two metals by means of rapid chemical reduction assisted by microwave heating. X-ray absorption spectroscopy suggested the formation of heteroatomic $Pd^{\delta+}Pt^{\delta-}$ sites *via* charge transfer between neighboring Pd and Pt atoms in the alloy structure. Moreover, Fourier transform IR spectroscopy and scanning transmission electron microscopy–energy-dispersive X-ray spectroscopy indicated that decreasing the size of the PdPt (50 : 50) nanoparticles improved the degree of alloying and facilitated the formation of electron-enriched $Pt^{\delta-}$ species. On the basis of kinetics studies and density functional theory calculations, we concluded that cyano group activation, which was the rate-determining step over monometallic Pd and Pt catalysts, was accelerated over the heteroatomic $Pd^{\delta+}Pt^{\delta-}$ sites because of strong back-donation from electron-enriched $Pt^{\delta-}$ species to the carbon atom of the cyano groups. The PdPt random alloy nanoparticles catalyzed the reactions of various aromatic and heterocyclic nitriles, and the corresponding secondary amines were selectively obtained in just a few hours.

Received 19th December 2021,
Accepted 28th February 2022

DOI: 10.1039/d1cy02302k

rsc.li/catalysis

1. Introduction

Secondary amines are versatile, indispensable intermediates in the production of pharmaceuticals, agrochemicals, and other bioactive chemicals, as well as rubber compounds and dyes.[1,2] Secondary amines are typically synthesized *via* N-alkylation and reductive amination,[3–15] but these reactions require expensive primary amines, toxic carbonyl compounds, and harsh reaction conditions. In addition, over-alkylation often occurs because of the high reactivity of amines and carbonyl compounds. As an alternative method, nitrile hydrogenation with gaseous hydrogen has recently been attracting attention because of its low material cost, high atom efficiency, and operational simplicity. During nitrile hydrogenation, the cyano group is sequentially hydrogenated to a primary amine. In addition, the primary amine product can be converted to a secondary imine or secondary amine *via in situ* condensation with the primary imine intermediate (Scheme 1). This chemodiversity makes controlling the

---

[a] *Department of Chemical Systems Engineering, Graduate School of Engineering, Nagoya University, Furo-cho, Chikusa-ku, Nagoya 464-8603, Japan. E-mail: nishida.yoshihide@nitech.ac.jp, sato.katsutoshi@material.nagoya-u.ac.jp, nagaoka.katsutoshi@material.nagoya-u.ac.jp*
[b] *Elements Strategy Initiative for Catalysts and Batteries, Kyoto University, 1-30 Goryo-Ohara, Nishikyo-ku, Kyoto 615-8245, Japan*
[c] *The Ultramicroscopy Research Center, Kyushu University, 744 Motooka, Nishi-ku, Fukuoka 819-0395, Japan*
[d] *Department of Applied Quantum Physics and Nuclear Engineering, Kyushu University, 744 Motooka, Nishi-ku, Fukuoka 819-0395, Japan*
[e] *National Institute of Technology, Akashi College, 679-3 Nishioka, Uozumi, Akashi, Hyogo 674-8501, Japan*
[f] *Advanced Ceramics Research Center, Nagoya Institute of Technology, 10-6-29 Asahigaoka, Tajimi, Gifu 507-0071, Japan*
[g] *Frontier Research Institute for Materials Science, Nagoya Institute of Technology, Gokiso-cho, Showa-ku, Nagoya 466-8555, Japan*

† Electronic supplementary information (ESI) available. See DOI: 10.1039/d1cy02302k

‡ (Present address) Advanced Ceramics Research Center, Nagoya Institute of Technology, 10-6-29 Asahigaoka, Tajimi, Gifu 507-0071, Japan.

§ (Present address) Renewable Energy Research Center, National Institute of Advanced Industrial Science and Technology, 2-2-9 Machiikedai, Koriyama, Fukushima 963-0298, Japan.

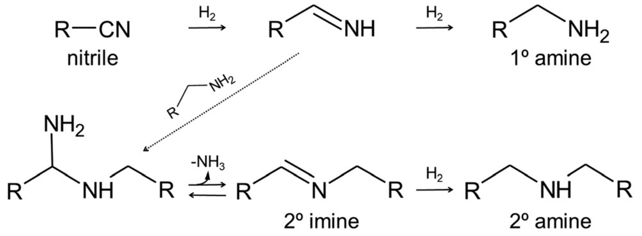

Scheme 1 Nitrile hydrogenation with gaseous hydrogen.

selectivity difficult, and the industrial RANEY® Ni and Co catalysts used for these reactions are unstable in air.[16] Therefore, considerable efforts have been devoted to developing new catalysts with high selectivity. For example, homogeneous Re, Ru, and Rh catalysts have been found to show high nitrile conversion and selectivity for secondary amines, albeit under harsh reaction conditions (60–140 °C and 10–75 bar).[17–19] In addition, heterogeneous Pd@mpg-C_3N_4 shows good conversion and selectivity for secondary amines at 80 °C and 10 bar,[20] and a Pt nanowire catalyst was found to convert various aromatic nitriles to their corresponding secondary amines at 80 °C and 1 bar.[21] Again, however, most of these newly reported catalysts require high temperature and/or hydrogen pressure, and nitrile hydrogenation under ambient conditions (room temperature and atmospheric pressure) remains challenging.

There have been a few reports on successful conversion of nitriles to secondary amines under ambient conditions, but high catalyst loads (>5 mol%) and long reaction times (24 h) are required.[22,23] The activity of catalysts can effectively be improved by bimetallization, which results in synergistic effects such as ligand and ensemble effects, in addition to allowing for concerted catalysis.[24–26] For example, a PtMo nanowire catalyst has been shown to be useful for converting aromatic nitriles to their corresponding secondary amines by hydrogenation at 80 °C and 1 bar.[27] A 5Pd–Ni/SiO_2 catalyst provides high conversion and selectivity for secondary amines at 80 °C and 6 bar.[28] In addition, a NiO–Pd/SiC catalyst (*ca.* 1 mol%) shows remarkable performance for the selective synthesis of secondary amines under mild conditions (30 °C and 1 bar), although a moderate reaction time (5 h) is required.[29]

Chemical reduction of metal precursors in the presence of polyvinylpyrrolidone (PVP) as a stabilizer is a simple and ecofriendly method for preparing metal nanoparticles, and the formation of well-dispersed Pd, Pt, and Pd/Pt nanoparticles has been reported.[30] PVP-stabilized bimetallic nanoparticle catalysts also show enhanced performance relative to that of monometallic catalysts.[31,32] In addition, the high dispersibility of PVP in polar protic solvents such as methanol may facilitate the diffusion of the reactants and PVP-stabilized nanoparticle catalysts in liquid-phase reactions and improve the reaction performance. Recently, we demonstrated for the first time that Rh nanoparticles stabilized by PVP effectively catalyze the selective formation of secondary imines from nitriles by hydrogenation under ambient conditions (25 °C and 1 bar).[33,34] Herein, we report an effective method for nitrile hydrogenation that affords secondary amines under ambient conditions over newly developed PdPt–PVP nanoparticle catalysts. Random alloying by chemical reduction generated PdPt–PVP nanoparticles, despite the fact that Pd and Pt are classically immiscible below 700 °C.[35,36] Small PdPt (50 : 50)–PVP nanoparticles (3.9 nm) catalyzed the conversion of various aromatic and heterocyclic nitriles to their corresponding secondary amines in a few hours, and the turnover frequency (TOF) was up to 10 times that achieved with monometallic Pd and Pt nanoparticles. Experimental and computational characterization of the catalysts revealed that the cyano groups were activated over heteroatomic $Pd^{\delta+}Pt^{\delta-}$ sites formed *via* charge transfer between neighboring Pd and Pt atoms in the random alloy structure.

2. Experiment

Materials

Metal precursors ($RuCl_3 \cdot nH_2O$, $RhCl_3 \cdot 3H_2O$, $(NH_4)_2PdCl_4$, $(NH_4)_2IrCl_6$, and $(NH_4)_2PtCl_4$), PVP K-30, ethylene glycol (EG), diethylether, acetone, methanol (MeOH), ethanol, and activated carbon were purchased from FUJIFILM Wako Pure Chemical Corporation (Japan) and Sigma Aldrich (United States of America). Nitrile compounds and dodecane were purchased from Tokyo Chemical Industry Co. (Japan). SiO_2 (OX-50) was obtained from NIPPON AEROSIL (Japan). All reagents were used as received.

Catalyst preparation

PVP-stabilized metal nanoparticles were synthesized by chemical reduction with an alcohol as a reductant. In a typical procedure, a sealable vessel was charged with 0.25 mmol metal precursors and 1.25 mmol PVP, and these reagents were dissolved in 20 mL of EG (Table S1†). Argon was bubbled through the solution to remove air, and then the vessel was sealed with a cap. In a microwave synthesizer (Initiator, Biotage, Sweden), the EG solution was rapidly heated to 165 °C and then maintained at that temperature for 15 min (Fig. S1†). After the EG solution was cooled, the resulting colloidal suspension was coagulated with diethyl ether and acetone, and the residual solid was washed three times by repeated dispersion in water and coagulation with diethyl ether and acetone. The washed product was dried under vacuum at 40 °C and crushed with an agate mortar. The morphology and particle-size distributions of the obtained nanoparticles were determined by transmission electron microscopy (TEM) (Fig. S2 and S3†). To vary the size of the PdPt (50 : 50) nanoparticles, we changed the total concentration of the metal precursors (Table S2 and Fig. S4–S6†). To vary the composition of the PdPt nanoparticles, we changed the ratio of the Pd and Pt precursors while keeping the total amount of the precursors at 0.25 mmol (Table S3 and Fig. S7 and S8†). For IR spectroscopy and applicability studies, the PdPt (50 : 50)–PVP nanoparticles were loaded onto SiO_2 and activated carbon supports by means of a conventional impregnation method; the metal loading was 5 wt%.

Hydrogenation of nitriles

Nitriles were hydrogenated in a test tube equipped with a gas bag. In a typical reaction, 1 mmol nitrile and 1 mol% catalyst were dispersed in 0.5 mL of MeOH. Then, the test tube was depressurized and filled with hydrogen gas at atmospheric pressure. The MeOH solution was stirred with a magnetic stirrer at 1200 rpm, and the reaction was allowed to proceed at 25 °C. Nitrile conversion and product yield were calculated by gas chromatography with flame ionization detection and dodecane as an internal standard. The obtained secondary amines were identified by means of gas chromatography-mass spectrometry.

3. Results and discussion

Catalytic performance of PVP-stabilized metal nanoparticles

We began by evaluating the catalytic performance of the PVP-stabilized metal nanoparticles in the hydrogenation of benzonitrile as a model substrate by using 1 bar of hydrogen at 25 °C (Table 1). The Ru and Ir nanoparticles showed low conversions (entries 1 and 2), probably because that the as-prepared nanoparticles were relatively small, they had inactive oxide surfaces that formed *via* air oxidation, and they were barely reduced during the hydrogenation reaction. The Rh and Pd nanoparticles showed 21% and 12% conversions and selectively gave *N*-benzylidenebenzylamine (**2**, secondary imine) and benzylamine (**1**, primary amine), respectively (entries 3 and 4). Hydrogenation over the Pt nanoparticles gave the desired dibenzylamine (**3**, secondary amine) as the major product, but the yield was only 9% (entry 5). Next, we tried bimetallization of the Pt nanoparticles to improve their catalytic activity, and we found that the nitrile conversion and target product yield dramatically increased when Pd was incorporated into the Pt nanoparticles (entry 6). The catalytic performance of the PdPt (50 : 50) nanoparticles strongly depended on the particle size, with the TOF increasing with decreasing particle size (entries 7–9). Note that the TOF over 3.9 nm PdPt (50 : 50) nanoparticles was approximately 10 times the TOFs over monometallic Pd and Pt nanoparticles. The origin of the particle-size dependence of TOF is discussed in a subsequent section. As a comparison experiment, we prepared physically mixed PdPt (50 : 50) nanoparticles by co-dispersing Pd–PVP and Pt–PVP nanoparticles, and we found that the catalytic performance of the physical mixture was lower than that of similarly sized bimetallic PdPt (50 : 50) nanoparticles (entry 10). This result indicates that the PdPt (50 : 50) nanoparticles were not composed simply of pure Pd and Pt domains and that bimetallization by chemical reduction was essential for the high catalytic performance.

Dependence of catalytic performance on the metal composition of PdPt nanoparticles

Next, we investigated the influence of the metal composition of the PdPt nanoparticles on their catalytic performance (Fig. 1 and Table S4†). We prepared PdPt nanoparticles with various metal compositions and found that they were spherical and well-dispersed (Fig. S7†). Notably, the sizes of the nanoparticles and amounts of included PVP varied within narrow ranges (Table S3 and Fig. S8†), which allowed us to easily determine the influence of metal composition on catalytic performance. Monometallic Pd nanoparticles showed little *in situ* condensation between the primary imine and primary amine, and then the selectivities for primary

Table 1 Hydrogenation of the model substrate benzonitrile to benzylamine (**1**), benzylidenebenzylamine (**2**), and dibenzylamine (**3**) under ambient conditions

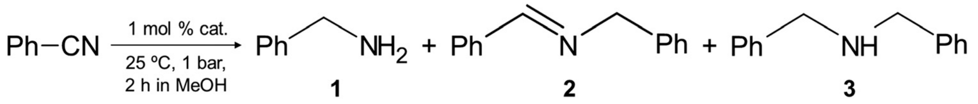

Entry	Catalyst	Particle size^a (nm)	Conv.^{b} (%)	Yield^b (%)			Dispersion^c (%)	TOF^d (h^{-1})
				1	**2**	**3**		
1	Ru–PVP	3.2	0	0	0	0	42	n/a
2	Ir–PVP	1.8	5	0	0	3	n/a	n/a
3	Rh–PVP	5.0	21	0	13	0	22	30 (21)
4	Pd–PVP	4.9	12	9	0	1	23	20 (12)
5	Pt–PVP	4.3	13	0	1	9	26	17 (13)
6	PdPt (50 : 50)–PVP	4.6	60	0	0	55	25	129 (23)
7	PdPt (50 : 50)–PVP	3.9	92	8	0	81	29	183 (16)
8	PdPt (50 : 50)–PVP	6.8	37	0	1	34	17	98 (19)
9	PdPt (50 : 50)–PVP	8.4	18	0	1	13	13	48 (18)
10	Pd + Pt (50 : 50)–PVP^e	4.9 + 4.3	35	17	0	15	n/a	n/a

[a] Particle size was determined by counting 200 particles in the TEM image of each catalyst. [b] Conversion and yield were calculated by means of gas chromatography with flame ionization detection using dodecane as an internal standard. [c] Metal dispersion was estimated according to the equation shown in Fig. S9,† on the assumption that the nanoparticles were spherical. [d] TOF was calculated from the metal dispersion and the yield of benzene rings at bracketed conversions. [e] Pd–PVP and Pt–PVP (entries 4 and 5) were co-dispersed in MeOH.

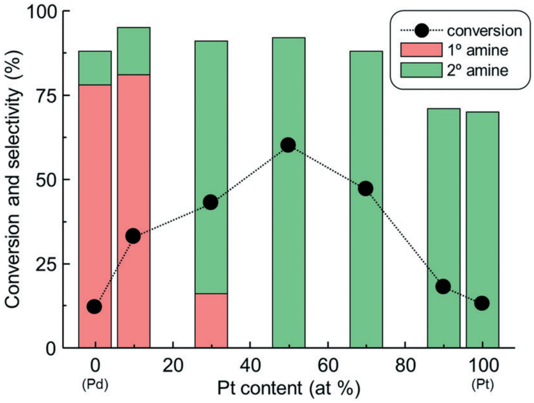

Fig. 1 Metal-composition dependence of the catalytic performance of the PdPt nanoparticles in the hydrogenation of benzonitrile (reaction conditions are shown in Table 1).

amine and secondary amine were 78% and 10%, respectively. On the other hand, the Pt nanoparticles catalyzed *in situ* condensation but their activity for the hydrogenation of secondary imine was low, and then 70% selectivity for secondary amine was obtained (Scheme 1). The selectivity of the PdPt (90:10) nanoparticles for the primary amine was comparable to that of monometallic Pd nanoparticles, indicating that the surface of the PdPt (90:10) nanoparticles was dominated by Pd species, which showed poor catalytic activity for *in situ* condensation. Conversely, the desired secondary amine was selectively obtained from reactions catalyzed by the PdPt nanoparticles containing at least 30% Pt, because Pt species, which facilitated the consumption of the primary amine *via in situ* condensation, were exposed on the surface of these nanoparticles. The PdPt (50:50) nanoparticles showed the highest selectivity for the desired secondary amine because they catalyzed not only *in situ* condensation but also the hydrogenation of secondary imine to secondary amine. In contrast, slightly lower secondary amine selectivity was observed with the Pt-enriched (>50%) nanoparticles, because their activity was insufficient to hydrogenate secondary imine to secondary amine. Moreover, the metal-composition dependence of benzonitrile conversion showed volcano-type behavior, with the highest conversion being obtained over the PdPt (50:50) nanoparticles. The time courses of substrate conversion and product yields over the PdPt (50:50) nanoparticles showed that the intermediates, including the primary amine, were rapidly transformed (Fig. S10†); the intermediates were undetectable even after a short reaction time, indicating that the hydrogenation of the cyano group was involved in the rate-determining step. If isolated Pd or Pt species surrounded by Pt or Pd, respectively, were active sites, then Pt- or Pd-enriched nanoparticles should show high activity.[26] In other words, our results suggest that the active sites were composed of Pd and Pt pairs.

To explore the effect of bimetallization on the catalytic activity of the PdPt (50:50) nanoparticles, several characterization techniques were carried out. We used scanning transmission electron microscopy combined with energy-dispersive X-ray spectroscopy (STEM–EDXS) to visualize the alloying state of the 4.6 nm PdPt (50:50) nanoparticles. Fig. 2 displays the high-angle annular dark-field images and elemental maps based on the Pd-L and Pt-L signals. In the high-resolution image, we observed the atomic arrangements of the ABCABC… stacking corresponding to the face-centered cubic structure (Fig. 2a). Additionally, the STEM–EDXS maps and an overlay image showed that the Pd-L and Pt-L signals were randomly distributed in a single particle, which means that the PdPt nanoparticles had a random alloy structure (Fig. 2c and d). The phase diagram for Pd and Pt indicates that they are thermodynamically immiscible below 700 °C,[35,36] but we nevertheless successfully synthesized the PdPt random alloy nanoparticles below 200 °C by chemical reduction using microwave

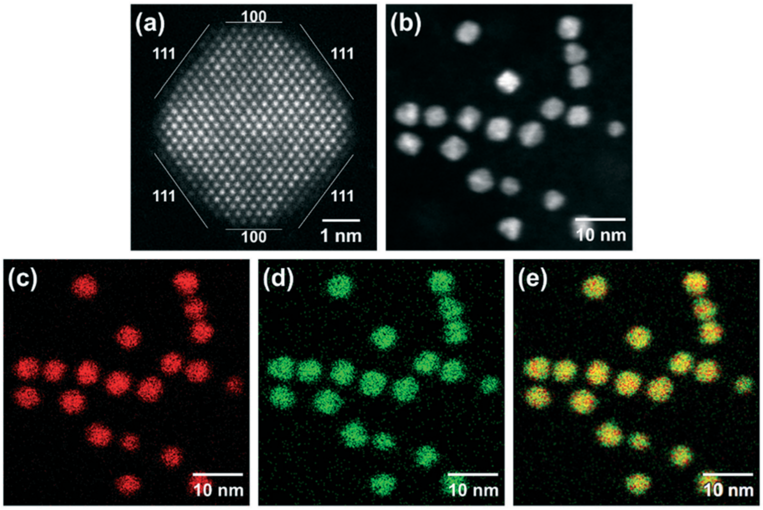

Fig. 2 (a) High-resolution high-angle annular dark-field image and (b) high-angle annular dark-field image. (c) Pd-L and (d) Pt-L maps obtained by STEM–EDXS analysis of the 4.6 nm PdPt (50:50) nanoparticles. (e) Overlay of the images in panels c and d.

heating. As a comparison experiment, we prepared the PdPt (50 : 50) nanoparticles under the conditions used for the preparation of the 4.6 nm sample, except that we employed a mantle heater, which allows for slow heating (1 °C min^{-1}, Fig. S11a†). The STEM–EDXS maps of the resulting nanoparticles showed that the Pd-L and Pt-L signals were localized at the interior and exterior of the particles, respectively (Fig. S11b–f†), which indicates the formation of a Pd-rich core and a Pt-rich surface phase. Furthermore, the small particles produced by heterogeneous heating from the mantle heater[34] were composed mainly of Pt species. On the basis of these experimental results, we propose that the alloying mechanism involves rapid and simultaneous reduction of the readily reducible $[PdCl_4]^{2-}$ and $[PtCl_4]^{2-}$ ions by microwave heating.

Next, we performed X-ray absorption spectroscopy at the SPring-8 synchrotron radiation facility. Fig. 3 shows the Pd K- and Pt L_3-edge X-ray absorption near-edge structure (XANES) spectra and the k^3-weighted Fourier transform (FT) extended X-ray absorption fine-structure (EXAFS) spectra of the PdPt nanoparticles with various metal compositions. The EXAFS oscillations before FT are also shown in Fig. S12.† In the XANES region, the white-line intensity of the Pt L_3-edge and the position of the Pd K-edge reflect the electronic states of the tested samples.[37,38] The Pd K- and Pt L_3-edge XANES spectra of the PdPt nanoparticles were similar to those of Pd and Pt foil, suggesting that at all metal compositions, the nanoparticles were composed of metallic Pd and Pt species (Fig. 3a and b). Notably, the white-line intensity of the Pt L_3-edge spectra decreased with increasing Pd content, which converted the Pt species to electron-enriched $Pt^{\delta-}$ species (Fig. 3b and S13†). In contrast, there was no significant change in the Pd K-edge XANES spectra with increasing Pt content, and evaluating the change in the electronic state of the Pd species with respect to the Pt content was difficult (Fig. 3a). This difficulty was probably due to the fact that the energy resolution at the Pd K-edge (24.4 keV) is lower than that at the Pt L_3-edge (11.5 keV).[39] However, density functional theory calculations described later in the paper suggest that the electron density of the Pd species decreased when the Pd atoms were replaced with Pt atoms, which means that the Pd species donated electrons to the Pt species in the PdPt nanoparticles. Additionally, the Pd K- and Pt L_3-edge FT EXAFS spectra, which provide information about the local coordination structure, depended on how much of the second element was introduced (Fig. 3c and d). The split peaks at 2–3 Å in the Pd K- and Pt L_3-edge spectra were attributed to the heteroatomic Pd–Pt bond,[40,41] which indicates that the PdPt nanoparticles had an alloy structure. In the X-ray diffraction analysis of the PdPt nanoparticles

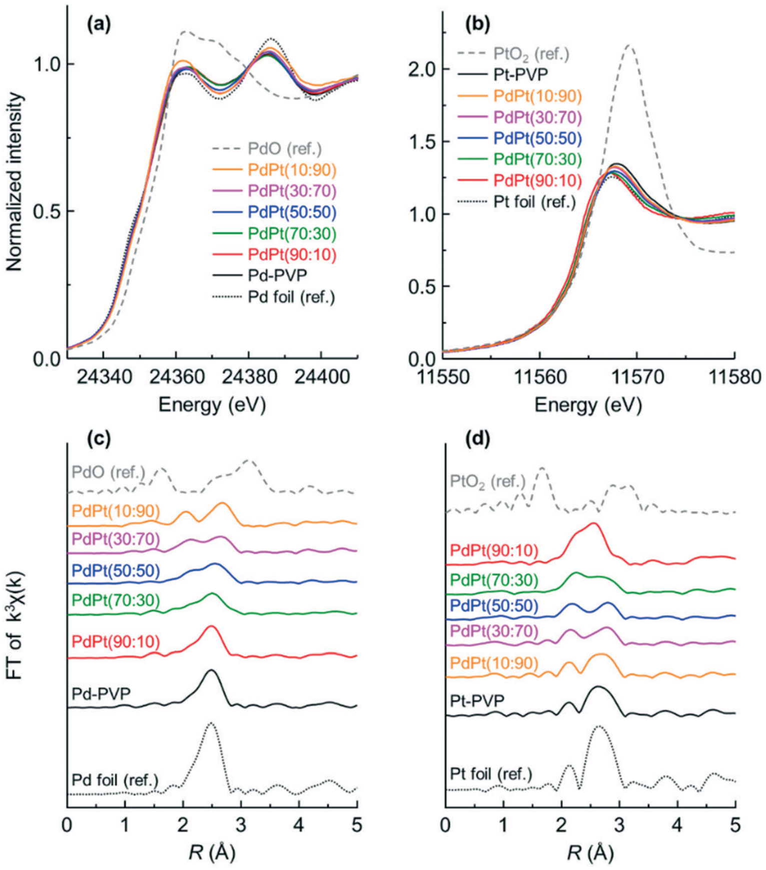

Fig. 3 (a) Pd K-edge and (b) Pt L_3-edge XANES spectra of the PdPt nanoparticles with various metal compositions. (c) Pd K-edge and (d) Pt L_3-edge FT EXAFS spectra of the PdPt nanoparticles with various metal compositions.

with various metal compositions (Fig. S14†), diffraction patterns attributed to a face-centered cubic structure were observed for all samples, which is consistent with the results of STEM–EDXS analysis (Fig. 2a). On the basis of the metal-composition dependence of the catalytic performance, STEM–EDXS analysis, and X-ray absorption spectroscopy, we propose that the hydrogenation of benzonitrile was promoted over heteroatomic $Pd^{\delta+}Pt^{\delta-}$ sites that formed *via* charge transfer between neighboring Pd and Pt atoms in the random alloy structure. Alloying equal amounts of Pd and Pt atoms maximized the number of heteroatomic $Pd^{\delta+}Pt^{\delta-}$ sites, resulting in excellent catalytic activity.

Particle-size dependence of the TOF over the PdPt (50 : 50) nanoparticles

To investigate the origin of the particle-size dependence of the TOF over the PdPt (50 : 50) nanoparticles (Table 1), we characterized the PdPt (50 : 50) nanoparticles by means of various methods. TEM showed that all the nanoparticle samples were well-dispersed with no aggregation, which indicates that any differences in the catalytic activity of the PdPt (50 : 50) nanoparticles could be attributed to the differences between their structures and electronic states. The surface states of the PdPt (50 : 50) nanoparticles, as well as monometallic Pt and Pd nanoparticles, were analyzed by FT-IR spectroscopy with carbon monoxide (CO) as a probe molecule (Fig. 4). The monometallic Pd nanoparticles showed a strong absorption peak assignable to CO adsorbed on bridge sites and three-fold hollow sites composed of metallic Pd species (Pd^0–CO_{bridge} and Pd^0–CO_{hollow}, respectively) at around 1750–1950 cm^{-1}.[24,42] Unfortunately, distinguishing between the Pd^0–CO_{bridge} and Pd^0–CO_{hollow} peaks was difficult because of the broadness of the peak. The monometallic Pt nanoparticles showed a strong peak at 2048 cm^{-1} and a weak peak at around 1750–1900 cm^{-1}; these peaks were assigned to CO adsorbed on linear and bridge sites composed of metallic Pt species, respectively (Pt^0–CO_{linear} and Pt^0–CO_{bridge}).[43,44] In contrast, the spectrum of the 3.9 nm PdPt (50 : 50) nanoparticles showed two representative absorption peaks: one at 2035 cm^{-1} and another at around 1750–1950 cm^{-1}. The former peak was assigned to Pt^0–CO_{linear}, and because the latter peak is located between the peaks observed for the monometallic Pd and Pt nanoparticles, it can probably be assigned to CO adsorbed on bridge and three-fold hollow sites composed of both Pd^0 and Pt^0 species. In other words, both Pd and Pt species were exposed and adjacent on the surface of the 3.9 nm PdPt (50 : 50) nanoparticles. Moreover, the wavenumber of the peak attributed to Pt^0–CO_{linear} (2035 cm^{-1}) was much lower than that observed for the monometallic Pt nanoparticles (2048 cm^{-1}), suggesting that the exposed Pt species were in an electron-enriched state owing to charge transfer from neighboring Pd species. However, the intensity of the peak at around 1750–1950 cm^{-1} gradually decreased as the size of the PdPt (50 : 50) nanoparticles increased, and the IR spectrum of CO adsorbed on the 8.4 nm PdPt (50 : 50) nanoparticles was quite similar to that of CO adsorbed on the monometallic Pt nanoparticles. These results suggest that increasing the size of the PdPt (50 : 50) nanoparticles reduced the degree of alloying, formed Pt-rich surfaces, and suppressed charge transfer. In other words, decreasing the particle size contributed to the formation of electron-enriched Pt species *via* random alloying, which in turn increased the catalytic activity and TOF.

To visualize the particle-size dependence of the degree of alloying, we performed STEM–EDXS analysis of the smallest (3.9 nm) and largest (8.4 nm) PdPt (50 : 50) nanoparticles. As expected, the homogeneous and heterogeneous distributions of the Pd-L and Pt-L signals were detected in the 3.9 nm sample (Fig. 4b–d) and the 8.4 nm sample (Fig. 4e–g), respectively. Particularly in the 8.4 nm sample, the Pd-L and Pt-L signals were localized at the interior and exterior of the particles, respectively, indicating the formation of a Pd-rich core and a Pt-rich surface phase (Fig. 4e–g). To improve the visibility of the structural differences between the 3.9 and 8.4

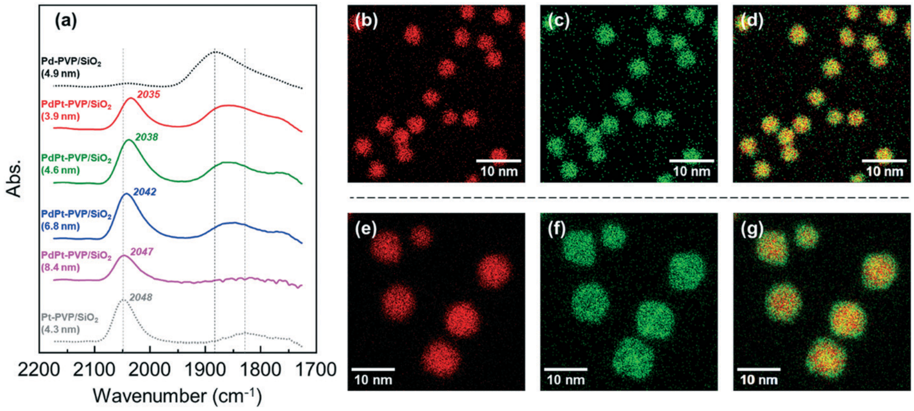

Fig. 4 (a) FT-IR spectra of CO adsorbed on the SiO_2-supported PdPt (50 : 50) nanoparticles of various sizes. (b) Pd-L and (c) Pt-L maps obtained by STEM–EDXS analysis of the 3.9 nm PdPt (50 : 50) nanoparticles. (d) Overlay of the images in panels b and c. (e) Pd-L and (f) Pt-L maps obtained by STEM–EDXS analysis of the 8.4 nm PdPt (50 : 50) nanoparticles. (g) Overlay of the images in panels e and f.

nm samples, we also recorded the line-scan profiles of the Pd-L and Pt-L signals. For the 3.9 nm sample, the Pd-L and Pt-L signals were randomly distributed around 50 at% regardless of the distance from the center of the particle, suggesting the formation of a random alloy structure (Fig. S15a†). In contrast, for the 8.4 nm sample, the Pd-L signals were higher at the particle interior than at the exterior and the Pt-L signals were higher at the exterior than at the interior (Fig. S15b†), meaning that increasing the size of the PdPt (50 : 50) nanoparticles led to the formation of particles with a Pd-rich core and a Pt-rich surface phase. Furthermore, we obtained the X-ray absorption spectra of the PdPt (50 : 50) nanoparticles of various sizes (Fig. S16 and S17†). The Pt L_3-edge XANES spectra showed that the particle size had no significant effect on the electronic state of bulk Pt species (Fig. S16b†), which suggests that changing the particle size did not affect the electron density of bulk Pt species. The results of XANES analysis cannot be compared with the results of FT-IR analysis, which provide information about the electronic state of the metal surface (Fig. 4). In addition, we observed no particle-size dependence in the Pd K-edge spectra because the energy resolution at the Pd K-edge is lower than that at the Pt L_3-edge (Fig. S16a†).[39] In the Pd K- and Pt L_3-edge FT EXAFS spectra, the split peaks attributed to the heteroatomic Pd–Pt bond were observed at 2–3 Å for all samples.[40,41] These experimental results show that increasing the particle size of the PdPt (50 : 50) nanoparticles resulted in structural changes at the particle surface rather than in the bulk. Considering that the size of the PdPt (50 : 50) nanoparticles changed when the concentration of the metal precursors was changed, we reasoned that the difference in the alloying degree arose from the collision and growth of the nanoparticles. That is, particle growth resulting from multiple collisions probably generated pure Pd and Pt domains under thermodynamic control.[35,36]

Mechanism of nitrile activation

To understand the reaction between benzonitrile and hydrogen over the 3.9 nm PdPt (50 : 50) random alloy and monometallic nanoparticles, we determined the influence of benzonitrile concentration and hydrogen pressure on the initial reaction rate (Fig. 5a and b). When the reaction was carried out over the monometallic Pd and Pt nanoparticles, the rate increased with increasing benzonitrile concentration and with increasing hydrogen pressure, and the obtained positive reaction orders for benzonitrile and hydrogen mean that their activation was involved in the rate-determining step. At a nitrile concentration higher than the original concentration, a negative reaction order was obtained over the Pt nanoparticles, suggesting that benzonitrile was strongly adsorbed on the surface of the Pt nanoparticles. In contrast, the reaction rate over the PdPt (50 : 50) nanoparticles was independent of nitrile concentration but strongly dependent on hydrogen pressure. These data demonstrate that the rate-determining step shifted from nitrile activation when the reaction was carried out over Pd and Pt to a step involving hydrogen when the reaction was carried out over a random alloy containing equal amounts of Pd and Pt atoms; that is, nitrile activation was strongly promoted over the PdPt (50 : 50) random alloy nanoparticles.

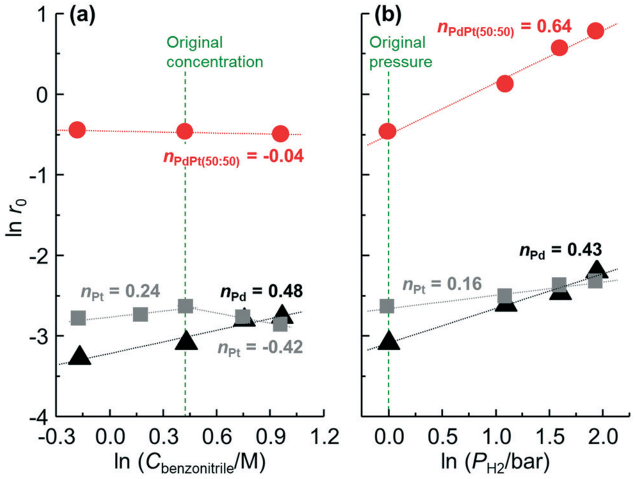

Fig. 5 Dependence of the initial reaction rate on (a) benzonitrile concentration and (b) hydrogen pressure over the 3.9 nm PdPt (50 : 50), 4.9 nm Pd, and 4.3 nm Pt nanoparticles. The reactions were performed under ambient conditions.

We carried out density functional theory calculations to clarify the mechanism of benzonitrile activation over the PdPt (50 : 50) nanoparticles. Fig. S18† shows a slab model of the nanoparticles and the corresponding histogram of the atomic charges. Clearly, the Pd species donated an electron to the Pt species; the average charges of the Pd and Pt atoms were +0.108*e* and −0.108*e*, respectively, which is consistent with the X-ray absorption spectroscopy and FT-IR results. Next, we calculated the benzonitrile adsorption sites on the 111 surface of the nanoparticles and found that in the stable adsorbed state, the cyano group was adsorbed on the bridge site and the plane of the aromatic ring was parallel to the 111 surface. In addition, the bridge-site dependence of the energy of adsorption on the PdPt (50 : 50) nanoparticles demonstrated that in the most stable state, the nitrogen and carbon atoms of the cyano group were located on the $Pd^{\delta+}$ and $Pt^{\delta-}$ atoms (labeled 02 in Fig. S19†); the atomic configuration of the most stable adsorbed benzonitrile molecule on the 111 surface of the PdPt (50 : 50) nanoparticles is shown in Fig. 6a. On the basis of the plausible adsorption configuration of benzonitrile on the 111 surface, we calculated the difference between the number of valence electrons on the carbon atom of the cyano group of adsorbed benzonitrile and the number on the carbon atom of gas-phase benzonitrile (Fig. 6b). In all the tested samples, the number of valence electrons increased owing to electron donation from the metal to the carbon atom (*i.e.*, back donation), and the PdPt (50 : 50) random alloy nanoparticles showed the largest change in the number of valence electrons. Note that the reaction orders for benzonitrile

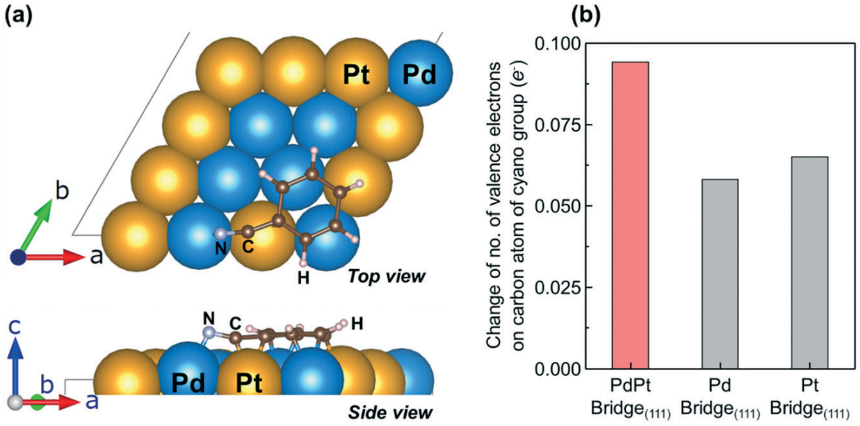

Fig. 6 (a) Most stable atomic configuration of benzonitrile adsorbed on the 111 surface of the PdPt (50 : 50) random alloy nanoparticles. Blue and yellow balls indicate the surface Pd and Pt atoms. Gray, brown, and white balls indicate nitrogen, carbon, and hydrogen atoms. The adsorption site is labeled 02 in Fig. S19.† The atoms were rendered using VESTA.[45] (b) The number of valence electrons on the carbon atom of the cyano group in the adsorbed benzonitrile compared with the number on the carbon atom in gas-phase benzonitrile. The numbers of valence electrons were determined by means of the Bader charge analysis.[46]

shown in Fig. 5 decreased with increasing the contribution of back donation (*i.e.*, nitrile activation). These results suggest that the back donation from the $Pt^{\delta-}$ atom of the heteroatomic $Pd^{\delta+}Pt^{\delta-}$ sites was strongly enhanced, which weakened the C≡N bond and thus enhanced the reactivity of the cyano group with dissociated hydrogen.

Reusability and applicability of 3.9 nm PdPt(50 : 50) nanoparticles

The reusability of the best-performing carbon-supported PdPt (50 : 50) nanoparticles (*i.e.*, the 3.9 nm nanoparticles) was evaluated in the hydrogenation of benzonitrile under ambient conditions. After the reaction for 3 h, the catalyst was collected by coagulation and centrifugation, washed with ethanol and diethylether, dried under vacuum at 40 °C, and then reused. These experiments revealed that the activity of the catalyst decreased with repeated use but the activity degradation slowed down after five uses (Fig. S20a†). Benzonitrile conversion stopped when the catalyst was removed from the reaction mixture by coagulation and centrifugation, which means that the active metal did not leach into the solution, and the catalytic reaction proceeded heterogeneously (Fig. S20b†). On the other hand, thermogravimetric analysis of the fresh and used carbon-supported catalysts showed that the metal loading decreased from 5.7 wt% to 4.2 wt% with repeated use (Fig. S21†), which may be due to the release of the metal particles from the carbon support by heavy stirring and shaking during catalyst washing. Additionally, TEM and STEM–EDXS analyses were used to directly observe the morphology of the catalyst before and after the reaction. Before the reaction, spherical nanoparticles were well-dispersed on the carbon support (Fig. S22a†). In contrast, after five uses, aggregates of the primary particles were observed although the size of the primary particles remained essentially unchanged (Fig. S22b and c and S23†). These results suggest that the decrease in catalytic activity with repeated use was due to a reduction in the number of exposed metal atoms (*i.e.*, available active sites) as a result of reduced metal loading and aggregate formation. Fortunately, the EDXS maps of the Pd-L and Pt-L signals clearly overlapped, indicating that the alloying state of the PdPt (50 : 50) nanoparticles was unchanged even after five uses (Fig. S22c–f†). In addition, the PdPt (50 : 50) nanoparticles that had been used five times showed better catalytic activity than the smaller Pd and Pt nanoparticles, owing to the alloying effect described in the above sections (Fig. S24†).

Next, we explored the applicability of the carbon-supported 3.9 nm PdPt (50 : 50) nanoparticles by carrying out reactions of various benzonitriles under ambient conditions (Table 2). Benzonitrile was successfully converted to its corresponding secondary amine in 96% yield after the reaction for 3 h (entry 1). Benzonitriles bearing an electron-withdrawing group ($-CF_3$, –F, or $-COCH_3$) afforded moderate to high yields of the corresponding secondary amines in only 2 h (entries 2–4), probably because the cyano groups in these substrates were strongly polarized by the electron-withdrawing functional group, which would favor the interaction with the heteroatomic $Pd^{\delta+}Pt^{\delta-}$ sites. In addition, benzonitriles with an electron-donating group ($-OCH_3$ or $-CH_3$) were transformed into secondary amines in 2–3 h (entries 5–7), which indicates that the interaction between the cyano group and the heteroatomic $Pd^{\delta+}Pt^{\delta-}$ sites was facilitated not only by electron-withdrawing functional groups but also by resonance structures involving the aromatic ring. Heterocyclic nitriles smoothly gave moderate to high yields of secondary amines (entries 8 and 9). In contrast, because of the lack of resonance effects, an aliphatic nitrile (isobutyronitrile) did not react completely even if the reaction time was prolonged (entry 10). It is notable that these newly developed PdPt (50 : 50) random alloy nanoparticles had higher catalytic activity for the hydrogenation of aromatic and

Table 2 Substrate scope of nitrile hydrogenation over the carbon-supported 3.9 nm PdPt (50 : 50) nanoparticles

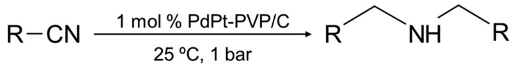

Entry	Substrate	Time (h)	Conv.[a] (%)	Yield[a] (%)
1	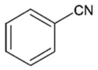	3	99	96
2	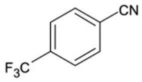	2	99	90
3	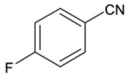	2	99	95
4	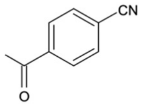	2	92	62
5	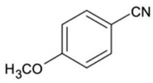	3	99	89
6	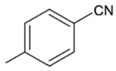	2	96	82
7	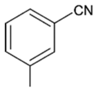	3	99	81
8	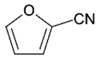	2	99	45
9	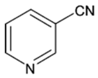	3	91	81
10	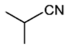	8	71	54

[a] Conversion and yield were calculated by gas chromatography with flame ionization detection using dodecane as an internal standard.

heterocyclic nitriles to the corresponding secondary amines than any previously reported catalysts (Table S5†).[17–23,27–29]

4. Conclusions

We found that benzonitriles can be effectively hydrogenated under ambient conditions over the newly developed bimetallic PdPt nanoparticles. Rapid chemical reduction assisted by microwave heating enabled us to randomly alloy classically immiscible Pd and Pt atoms, resulting in a markedly enhanced catalytic activity relative to that of monometallic Pd and Pt catalysts; nitrile hydrogenation reactions catalyzed by the alloyed catalysts selectively produced secondary amines. Experimental and computational studies revealed that the hydrogenation reaction was accelerated over heteroatomic $Pd^{\delta+}Pt^{\delta-}$ sites because of strong back-donation. In addition, alloying equal amounts of Pd and Pt atoms and decreasing the size of the nanoparticles maximized the number of heteroatomic $Pd^{\delta+}$-$Pt^{\delta-}$ sites, resulting in the formation of electron-enriched $Pt^{\delta-}$ species, and thus enhanced catalytic activity. The nanoparticles could be used to transform various aromatic and heterocyclic nitriles into their corresponding secondary amines in just a few hours under ambient conditions. Our findings can be expected to facilitate the development of a new class of catalysts that will enable molecular transformations without the need for heat, pressurization, or long reaction times.

Author contributions

Yoshihide Nishida: designing of research, data collection, and writing-editing. Katsutoshi Sato: coordination of characterization, conducting X-ray absorption spectroscopy, and editing. Chandan Chaudhari and Hiroshi Yamada: data curation and validation. Takaaki Toriyama, Tomokazu Yamamoto and Syo Matsumura: STEM–EDXS analysis. Susan Meñez Aspera and Hiroshi Nakanishi: density functional theory calculation. Masaaki Haneda: FT-IR analysis. Katsutoshi Nagaoka: designing of research and writing-editing.

Conflicts of interest

There are no conflicts to declare.

Acknowledgements

This research was supported by the ACCEL program, Japan Science and Technology Agency (JST), JPMJAC1501 and the Japan Society for the Promotion of Science (JSPS) KAKENHI, 20J13035. STEM observations were performed as a part of a program conducted by the Advanced Characterization Nanotechnology Platform Japan, sponsored by the Ministry of Education, Culture, Sports, Science and Technology (MEXT), Japan (No. JPMXP09A20KU0356). X-ray absorption measurements were performed at the BL01B1 facilities of SPring-8 at the approval of the Japan Synchrotron Radiation Research Institute (JASRI) (Nos. 2019A1703 and 2020A1692). K. Sato thanks the Program for Elements Strategy Initiative for Catalysts & Batteries (ESICB) commissioned by MEXT. We acknowledge Dr. K. Kusada and Dr. H. Asakura (Kyoto University) for fruitful discussions concerning X-ray diffraction and X-ray absorption analysis.

References

1 C. Su, R. Tandiana, J. Balapanuru, W. Tang, K. Pareek, C. T. Nai, T. Hayashi and K. P. Loh, *J. Am. Chem. Soc.*, 2015, **137**, 685–690.
2 P. P. Zhao, X. F. Zhou, J. J. Dai and H. J. Xu, *Org. Biomol. Chem.*, 2014, **12**, 9092–9096.
3 R. N. Salvatore, A. S. Nagle, S. E. Schmidt and K. W. Jung, *Org. Lett.*, 1999, **1**, 1893–1896.
4 G. Marzaro, A. Guiotto and A. Chilin, *Green Chem.*, 2009, **11**, 774–776.
5 M. C. Lubinu, L. De Luca, G. Giacomelli and A. Porcheddu, *Chem. – Eur. J.*, 2011, **17**, 82–85.

6 M. H. S. A. Hamid, P. A. Slatford and J. M. J. Williams, *Adv. Synth. Catal.*, 2007, **349**, 1555–1575.

7 C. Chiappe and D. Pieraccini, *Green Chem.*, 2003, **5**, 193–197.

8 O. Saidi, A. J. Blacker, M. M. Farah, S. P. Marsden and J. M. Williams, *Chem. Commun.*, 2010, **46**, 1541–1543.

9 O. Saidi, A. J. Blacker, M. M. Farah, S. P. Marsden and J. M. Williams, *Angew. Chem., Int. Ed.*, 2009, **48**, 7375–7378.

10 T. T. Dang, B. Ramalingam, S. P. Shan and A. M. Seayad, *ACS Catal.*, 2013, **3**, 2536–2540.

11 B. Emayavaramban, P. Chakraborty, E. Manoury, R. Poli and B. Sundararaju, *Org. Chem. Front.*, 2019, **6**, 852–857.

12 R. Apodaca and W. Xiao, *Org. Lett.*, 2001, **3**, 1745–1748.

13 S. Hoffmann, M. Nicoletti and B. List, *J. Am. Chem. Soc.*, 2006, **128**, 13074–13075.

14 A. F. Abdel-Magid, K. G. Carson, B. D. Harris, C. A. Maryanoff and R. D. Shah, *J. Org. Chem.*, 1996, **61**, 3849–3862.

15 J. S. Sapsford, D. J. Scott, N. J. Allcock, M. J. Fuchter, C. J. Tighe and A. E. Ashley, *Adv. Synth. Catal.*, 2018, **360**, 1066–1071.

16 T. Mitsudome, M. Sheng, A. Nakata, J. Yamasaki, T. Mizugaki and K. Jitsukawa, *Chem. Sci.*, 2020, **11**, 6682–6689.

17 K. Rajesh, B. Dudle, O. Blacque and H. Berke, *Adv. Synth. Catal.*, 2011, **353**, 1479–1484.

18 S. Saha, M. Kaur, K. Singh and J. K. Bera, *J. Organomet. Chem.*, 2016, **812**, 87–94.

19 Y. Sato, Y. Kayaki and T. Ikariya, *Organometallics*, 2016, **35**, 1257–1264.

20 Y. Li, Y. Gong, X. Xu, P. Zhang, H. Li and Y. Wang, *Catal. Commun.*, 2012, **28**, 9–12.

21 S. Lu, J. Wang, X. Cao, X. Li and H. Gu, *Chem. Commun.*, 2014, **50**, 3512–3515.

22 A. Galan, J. De Mendoza, P. Prados, J. Rojo and A. M. Echavarren, *J. Org. Chem.*, 1991, **56**, 452–454.

23 Y. Monguchi, M. Mizuno, T. Ichikawa, Y. Fujita, E. Murakami, T. Hattori, T. Maegawa, Y. Sawama and H. Sajiki, *J. Org. Chem.*, 2017, **82**, 10939–10944.

24 N. Toshima and T. Yonezawa, *New J. Chem.*, 1998, **22**, 1179–1201.

25 Y. Nakagawa and K. Tomishige, *Catal. Commun.*, 2010, **12**, 154–156.

26 H. Miura and T. Shishido, *Chem. Lett.*, 2021, **50**, 346–352.

27 S. Lu, P. Xu, X. Cao and H. Gu, *RSC Adv.*, 2018, **8**, 8755–8760.

28 H. Wang, Q. Luo, W. Liu, Y. Lin, Q. Guan, X. Zheng, H. Pan, J. Zhu, Z. Sun, S. Wei, J. Yang and J. Lu, *Nat. Commun.*, 2019, **10**, 4998–5006.

29 Z.-F. Jiao, J.-X. Zhao, X.-N. Guo, X.-L. Tong, B. Zhang, G.-Q. Jin, Y. Qin and X.-Y. Guo, *Catal. Sci. Technol.*, 2019, **9**, 2266–2272.

30 M. Yamauchi, H. Kobayashi and H. Kitagawa, *ChemPhysChem*, 2009, **10**, 2566–2576.

31 K. Kusada, H. Kobayashi, R. Ikeda, Y. Kubota, M. Takata, S. Toh, T. Yamamoto, S. Matsumura, N. Sumi, K. Sato, K. Nagaoka and H. Kitagawa, *J. Am. Chem. Soc.*, 2014, **136**, 1864–1871.

32 C. Song, A. Tayal, O. Seo, J. Kim, Y. Chen, S. Hiroi, L. S. R. Kumara, K. Kusada, H. Kobayashi, H. Kitagawa and O. Sakata, *Nanoscale Adv.*, 2019, **1**, 546–553.

33 Y. Nishida, C. Chaudhari, H. Imatome, K. Sato and K. Nagaoka, *Chem. Lett.*, 2018, **47**, 938–940.

34 Y. Nishida, Y. Wada, C. Chaudhari, K. Sato and K. Nagaoka, *J. Jpn. Pet. Inst.*, 2019, **62**, 220–227.

35 S. R. Bharadwaj, A. S. Kerkar, S. N. Tripathi and S. R. Dharwadkar, *J. Less-Common Met.*, 1991, **169**, 167–172.

36 G. Rakhtsaum, *Platinum Met. Rev.*, 2013, **57**, 202–213.

37 C. Sarkar, P. Koley, I. Shown, J. Lee, Y.-F. Liao, K. An, J. Tardio, L. Nakka, K.-H. Chen and J. Mondal, *ACS Sustainable Chem. Eng.*, 2019, **7**, 10349–10362.

38 L. S. R. Kumara, O. Sakata, H. Kobayashi, C. Song, S. Kohara, T. Ina, T. Yoshimoto, S. Yoshioka, S. Matsumura and H. Kitagawa, *Sci. Rep.*, 2017, **7**, 14606.

39 H. Miura, K. Endo, R. Ogawa and T. Shishido, *ACS Catal.*, 2017, **7**, 1543–1553.

40 N. Toshima, M. Harada, T. Yonezawa, K. Kushihashi and K. Asakura, *J. Phys. Chem.*, 1991, **95**, 7448–7453.

41 C. Cong, S. Nakayama, S. Maenosono and M. Harada, *Ind. Eng. Chem. Res.*, 2018, **57**, 179–190.

42 J. Prinz, R. Gaspari, Q. S. Stöckl, P. Gille, M. Armbrüster, H. Brune, O. Gröning, C. A. Pignedoli, D. Passerone and R. Widmer, *J. Phys. Chem. C*, 2014, **118**, 12260–12265.

43 E. S. Gutterød, S. Øien-Ødegaard, K. Bossers, A.-E. Nieuwelink, M. Manzoli, L. Braglia, A. Lazzarini, E. Borfecchia, S. Ahmadigoltapeh, B. Bouchevreau, B. T. Lønstad-Bleken, R. Henry, C. Lamberti, S. Bordiga, B. M. Weckhuysen, K. P. Lillerud and U. Olsbye, *Ind. Eng. Chem. Res.*, 2017, **56**, 13206–13218.

44 M. J. Hossain, M. M. Rahman and M. Jafar Sharif, *Nanoscale Adv.*, 2020, **2**, 1245–1252.

45 K. Momma and F. Izumi, *J. Appl. Crystallogr.*, 2011, **44**, 1272–1276.

46 G. Henkelman, A. Arnaldsson and H. Jónsson, *Comput. Mater. Sci.*, 2006, **36**, 354–360.